



Understanding Broad Mg II Variability in Quasars with Photoionization: Implications for Reverberation Mapping and Changing-look Quasars

Hengxiao Guo (郭恒潇)^{1,2} , Yue Shen^{1,2,8} , Zhicheng He^{3,4} , Tinggui Wang^{3,4} , Xin Liu^{1,2} , Shu Wang^{5,6},
Mouyuan Sun^{3,4} , Qian Yang^{1,2} , Minzhi Kong^{1,7}, and Zhenfeng Sheng^{3,4}

¹ Department of Astronomy, University of Illinois at Urbana-Champaign, Urbana, IL 61801, USA; hengxiao@illinois.edu, shenyue@illinois.edu

² National Center for Supercomputing Applications, University of Illinois at Urbana-Champaign, Urbana, IL 61801, USA

³ CAS Key Laboratory for Researches in Galaxies and Cosmology, University of Sciences and Technology of China, Hefei, Anhui 230026, People's Republic of China

⁴ School of Astronomy and Space Science, University of Science and Technology of China, Hefei 230026, People's Republic of China

⁵ Kavli Institute for Astronomy and Astrophysics, Peking University, Beijing 100871, People's Republic of China

⁶ Department of Astronomy, School of Physics, Peking University, Beijing 100871, People's Republic of China

⁷ Department of Physics, Hebei Normal University, No. 20 East of South 2nd Ring Road, Shijiazhuang 050024, People's Republic of China

Received 2019 July 15; revised 2019 November 6; accepted 2019 November 26; published 2020 January 8

Abstract

The broad Mg II line in quasars has distinct variability properties compared with broad Balmer lines: it is less variable and usually does not display a “breathing” mode, the increase in the average cloud distance when luminosity increases. We demonstrate that these variability properties of Mg II can be reasonably well explained by simple locally optimally emitting cloud (LOC) photoionization models, confirming earlier photoionization results. In the fiducial LOC model, the Mg II-emitting gas is on average more distant from the ionizing source than the H α /H β gas and responds with a lower amplitude to continuum variations. If the broad-line region (BLR) is truncated at a physical radius of ~ 0.3 pc (for a $10^{8.5} M_{\odot}$ BH accreting at Eddington ratio of 0.1), most of the Mg II flux will always be emitted near this outer boundary and hence will not display breathing. These results indicate that reverberation mapping results on broad Mg II, while generally more difficult to obtain owing to the lower line responsivity, can still be used to infer the Mg II BLR size and hence black hole mass. But it is possible that Mg II does not have a well-defined intrinsic BLR size–luminosity relation for individual quasars, even though a global one for the general population may still exist. The dramatic changes in broad H α /H β emission in the observationally rare changing-look quasars are fully consistent with photoionization responses to extreme continuum variability, and the LOC model provides natural explanations for the persistence of broad Mg II in changing-look quasars defined on H α /H β and the rare population of broad Mg II emitters in the spectra of massive inactive galaxies.

Unified Astronomy Thesaurus concepts: Active galactic nuclei (16); Quasars (1319); Black hole physics (159); Reverberation mapping (2019)

1. Introduction

The ubiquitous aperiodic variability of quasars can be utilized to probe different spatial scales, for example, to measure the size of the broad-line region (BLR) and hence to estimate the black hole (BH) mass. The origin of quasar continuum variability could be changes in the accretion rate (e.g., Li & Cao 2008), or complex disk instabilities (e.g., Lyubarskii 1997; Dexter & Agol 2011; Cai et al. 2016). The delayed responses of more extended emitting regions (such as the BLR) to the continuum variations measure the characteristic distance of these emitting regions to the central BH ($R = c\tau$, where τ is the time lag between continuum and broad-line variability and c is the speed of light), a technique known as reverberation mapping (RM; Blandford & McKee 1982; Peterson 2014). Combined with the broad-line width ΔV (a proxy for the virial velocity in the BLR) measured from spectroscopy, one can estimate the BH mass as

$$M_{\text{BH}} = \frac{f \Delta V^2 R}{G}, \quad (1)$$

where f is a scale factor of order unity that accounts for the BLR orientation, kinematics, structure, and other unknown

factors, and G is the gravitational constant. So far there have been more than 60 low-redshift ($z < 0.3$) active galactic nuclei (AGNs) with successful RM lag measurements (e.g., Kaspi et al. 2000; Peterson et al. 2004; Barth et al. 2015; Du et al. 2016; see also a recent compilation of the RM BH mass database from Bentz & Katz 2015), mostly for the broad H β line. These measurements have revealed a scaling relation between the size of the BLR and the continuum luminosity (i.e., $R \propto L^{0.5}$; e.g., Kaspi et al. 2000; Bentz et al. 2006) for H β , which is naively expected from photoionization, i.e., $R \propto L_{\text{ion}}^{0.5}$, where L_{ion} is the hydrogen-ionizing luminosity in photoionization models (e.g., Korista & Goad 2000). This R – L relation underlies the BH mass estimation with single-epoch spectroscopy, using luminosity as a proxy for the BLR size (e.g., Shen 2013).

At $1 \lesssim z \lesssim 2$, the strong Balmer lines H α and H β shift out of the optical band, and Mg II becomes the major broad line of interest for RM with optical spectroscopy. Compared with the Balmer lines, results on Mg II RM are scarce and more ambiguous. Only in a handful cases has an Mg II lag been robustly detected (Clavel et al. 1991; Reichert et al. 1994; Metzroth et al. 2006; Shen et al. 2016; Czerny et al. 2019), with many attempts failing to result in a detection (Trevese et al.

⁸ Alfred P. Sloan Research Fellow.

2007; Woo 2008; Hryniewicz et al. 2014; Cackett et al. 2015). Part of the difficulty of Mg II lag detection is the apparently lower variability amplitude of Mg II compared to the Balmer lines in the same objects (e.g., Sun et al. 2015).

Extensive earlier theoretical works on photoionization have suggested that Mg II has not only a weaker response to continuum variations, resulting in weaker line variability, but also a larger average formation radius, compared to Balmer lines (Goad et al. 1993; O’Brien et al. 1995; Korista & Goad 2000; Goad et al. 2012). Based on the *International Ultraviolet Explorer (IUE)* (monitoring of the Seyfert 1 galaxy NGC 4151, Metzroth et al. (2006) reported a reliable Mg II time lag ($\tau \sim 5\text{--}7$ days) but weak line variability—the fractional Mg II line variability is less than 30% of that for the continuum around 1355 Å. Similarly, Clavel et al. (1991) detected a marginal Mg II lag in NGC 5548 with weak line variability (the fractional Mg II variability is only $\sim 30\%$ with respect to continuum). Cackett et al. (2015) also attempted Mg II RM in NGC 5548 with *Swift* spectra sampled every 2 days in 2013. However, there was no significant Mg II lag detected given the weak Mg II variability. Other studies of individual objects also confirmed the general weak variability of Mg II, e.g., NGC 3516 (Goad et al. 1999a, 1999b), PG 1634+706 and PG 1247+268 (Trevese et al. 2007), and CTS C30.10 (Modzelewska et al. 2014). In addition, population studies of quasar variability in the Sloan Digital Sky Survey (SDSS) Stripe 82 and SDSS-RM (Shen et al. 2015) also found that Mg II variability is generally weaker than those from Balmer lines (Kokubo et al. 2014; Sun et al. 2015). Studies of the broad-line responses to large-amplitude continuum variations (more than 1 mag) over multiyear timescales also confirmed that the Mg II response to continuum is much weaker than that for the broad Balmer lines (Yang et al. 2019). Meanwhile, the predicted relatively larger Mg II formation radius than the Balmer lines is also consistent with limited RM results where both the Mg II and Balmer line lags are available (e.g., Clavel et al. 1991; Peterson & Wandel 1999; Shen et al. 2016; Grier et al. 2017).

On the other hand, intense RM monitoring of the broad Balmer lines has revealed a “breathing mode” of the line (Gilbert & Peterson 2003; Korista & Goad 2004; Cackett & Horne 2006; Denney et al. 2009; Park et al. 2012; Barth et al. 2015; Runco et al. 2016): as the central luminosity increases, more distant clouds can be photoionized to produce broad-line emission, and the broad-line width (inversely related to the emissivity-weighted radius) decreases, and vice versa. Assuming that the BLR is virialized, we expect that the line width $\Delta V \propto L^{-0.25}$ assuming $R \propto L^{0.5}$ as for the H β BLR.

The “breathing” mode for broad Mg II has not been well studied. Recently, Yang et al. (2019) studied 16 extreme variability quasars with spectroscopy covering Mg II and found that the line width of Mg II does not vary accordingly as continuum varies by more than a factor of few for most objects (see their Figure 4), in contrast to the well-known “breathing” model for H β . Similar results are reported in Shen (2013) for a large sample of quasars with two-epoch spectroscopy to probe the continuum and broad-line variability. This is somewhat surprising, given that Mg II is also a low-ionization line like the Balmer lines and that the average Mg II width correlates well with that of H β for the population of quasars (Shen et al. 2008, 2011). In rare cases reported, however, Mg II may also display breathing, albeit to a lesser degree compared to H β (e.g., Dexter et al. 2019).

Given the importance of broad Mg II for RM at intermediate redshifts and for understanding quasar BLRs in general, it is important for us to understand Mg II variability. Unlike the recombination lines (e.g., H β and H α), Mg II is mostly collisionally excited. To fully understand the different variability properties of broad Mg II, detailed photoionization calculations are required. In this work we construct photoionization models using CLOUDY (Ferland et al. 2017, version 17.01) to understand Mg II variability and compare to the Balmer lines. In Section 2, we discuss the excitation and emission mechanisms of different lines. In Section 3 we confirm the low intrinsic response and large formation radius for Mg II with respect to Balmer lines in the LOC picture (e.g., Goad et al. 1993; O’Brien et al. 1995; Korista & Goad 2000; Goad et al. 2012). In Section 4, we discuss the implications of Mg II variability on RM and present a sequence of “changing-look” in Balmer lines and Mg II as the continuum luminosity undergoes significant variations. We summarize our findings in Section 5.

2. Emission Mechanisms for H α , H β , and Mg II

In order to investigate the variability behaviors of the three different broad lines, we first need to understand their excitation and emission mechanism and response to the central ionizing source. H α and H β are recombination lines in the BLR with large column density ($\sim 10^{23}$ cm $^{-2}$) and high volume density ($\sim 10^{10}$ cm $^{-3}$) clouds. The ionization potential of H I is 13.6 eV, and the ionized H I will subsequently recombine and emit Balmer lines (e.g., H β and H α) in ionization equilibrium. The recombination timescale is given by

$$\tau_{\text{rec}} = (n_e \alpha)^{-1} \sim 0.1(10^{10} \text{ cm}^{-3}/n_e)\text{hr}, \quad (2)$$

which is related to the recombination coefficient α and the electron density n_e . Assuming $n_e = 10^{10}$ cm $^{-3}$, it yields a recombination timescale of a few minutes.

Unlike Balmer lines, Mg II is dominated by collisional excitation given its low excitation energy (4.4 eV). The ionization energy of Mg II to Mg III is >15 eV (comparable to the 13.6 eV ionization energy of H I), which indicates a similar emissivity-weighted radius to that of the Balmer lines, whereas the magnesium abundance ($Z = \log N_{\text{MgII}}/N_{\text{H}} + 12 = 7.58$, where N is the column density of different elements) is four orders of magnitude lower than hydrogen ($Z = Z_{\odot}$). Therefore, the contribution from recombination is negligible for Mg II emission. The collisional timescale of Mg II is given by

$$\tau_{\text{col}} = \left(\frac{8.63 \times 10^{-6} n_e \gamma_{\text{mn}} \exp(-\chi_{\text{mn}}/kT)}{\omega_m T_e^{0.5}} \right)^{-1} \text{ s}, \quad (3)$$

where $\gamma_{\text{mn}} = 16.9$ is the collisional strength for $3p^2P^0 - 3s^2S^0$ transitions, k is the Boltzmann constant, the statistical weight ω_m is 6 for $3p^2P^0$, and $\chi_{\text{mn}} = E_m - E_n = 4.4$ eV for Mg II resonance transition (Osterbrock 1989). Assuming gas electron temperature $T_e = 10^4$ K and $n_e = 10^{10}$ cm $^{-3}$, we obtain the approximate collisional timescale of ~ 0.01 s.

Figure 1 presents various cloud parameters as a function of column density in the simple one-cloud model. We assume that a slab cloud in an open geometry, with ionization parameter $\log U_{\text{H}} = -1$, a column density of $N_{\text{H}} = 10^{25}$ cm $^{-2}$, and solar abundance $Z = Z_{\odot}$, is irradiated on one side by a typical radio-

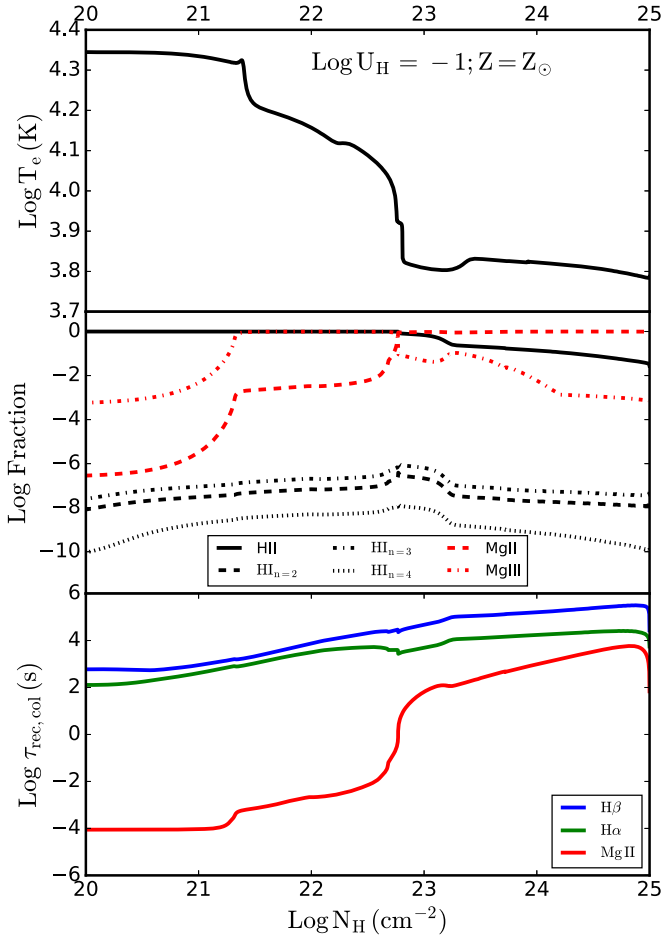


Figure 1. Electron temperature, atom/ion number density fractions, and excitation timescales as a function of column density. We adopt a simple one-cloud model with typical BLR parameters, i.e., ionization parameter $\log U_{\text{H}} = -1$ and chemical abundance $Z = Z_{\odot}$. We perform radiative transfer calculations up to $N_{\text{H}} = 10^{25} \text{ cm}^{-2}$. In the top panel, the electron temperature decreases with increasing hydrogen column density. The middle panel shows the ionization states of hydrogen and magnesium as a function of total column density. Mg II has its significant production around $N_{\text{H}} = 10^{23} \text{ cm}^{-2}$ since its abundance (emitting efficiency) increases (decreases) with the hydrogen column density. The bottom panel shows the recombination timescales of H β and H α and the collisional timescale of Mg II, which are consistent with the estimation from Equations (2) and (3).

quiet AGN spectral energy distribution (SED) with the big blue bump (Mathews & Ferland 1987). As column density increases, the electron temperature drops (top panel), and Mg II abundance starts to exceed that of Mg III above $N_{\text{H}} \sim 10^{22.7} \text{ cm}^{-2}$, i.e., Mg II is not overionized at sufficiently high column densities (middle panel). However, the Mg II-emitting efficiency will decrease at very high hydrogen column density (e.g., 10^{25} cm^{-2} corresponds to Compton-thick clouds), resulting in that Mg II emission reaches peak production around $N_{\text{H}} \sim 10^{23} \text{ cm}^{-2}$. The hydrogen abundances at different energy levels are relatively constant. In the bottom panel, we show that the timescales (τ_{rec} of recombination and τ_{col} of collisional excitation) are much smaller than 1 day and hence negligible compared with the time delay in BLR response or the interval of multipoch observations.

In the next section, we use photoionization results calculated for individual clouds to construct more realistic BLR models that cover a distribution in cloud properties with a spherically symmetric geometry.

3. LOC Models

A physically motivated photoionization model for the BLR is the locally optimally emitting cloud (LOC) model, which consists of clouds with different gas densities and distances from the central continuum source with an axisymmetric distribution (Baldwin et al. 1995). In this model, the line emission we observe originates from the combination of all clouds but is dominated by those with the highest efficiency of reprocessing the incident ionizing continuum, i.e., those clouds with the optimal distance from the central source and gas density. This natural selection effect is due to a combination of ionization potential, collisional de-excitation of the upper levels, and thermalization at large optical depths.

In the following sections, we will consider a typical quasar at $z = 0.5$ with $M_{\text{BH}} = 10^{8.5} M_{\odot}$ and $L_{3000\text{\AA}} = 10^{44} - 10^{45} \text{ erg s}^{-1}$ (or $Q(\text{H}) \simeq 10^{54.5} - 10^{55.5} (\text{s}^{-1})$),⁹ corresponding to Eddington ratios $L_{\text{bol}}/L_{\text{Edd}} \sim 0.01 - 0.1$. The high Eddington ratio ($L_{\text{bol}}/L_{\text{Edd}} \sim 0.1$) represents the typical Eddington ratio observed in quasars (e.g., Shen et al. 2011), and the low Eddington ratio ($L_{\text{bol}}/L_{\text{Edd}} \sim 0.01$) represents the state where the quasar has significantly dimmed in accretion luminosity. We still use the same radio-quiet AGN SED in Mathews & Ferland (1987) for the incident SED.

Consider the best-studied AGN NGC 5548 (e.g., Korista & Goad 2000), which has an average $Q(\text{H}) = 10^{54.13} \text{ s}^{-1}$ and an outer BLR boundary of about 140 lt-day, determined by dust sublimation of the inner edge of the torus with a surface ionizing flux $\log \Phi(\text{H}) \simeq 17.9 (\text{cm}^{-2} \text{ s}^{-1})$ (Nenkova et al. 2008; Landt et al. 2019). Scaling to the average luminosity of $10^{44.5} \text{ erg s}^{-1}$ at 3000 Å for our quasar, we determine an outer BLR boundary of $R_{\text{out}} = 10^{18} \text{ cm}$ (since $Q(\text{H}) = 4\pi R^2 \Phi(\text{H})$; see Equation (4)). For completeness, the other parameters used in our fiducial LOC model are the inner BLR boundary $R_{\text{in}} = 10^{16.5} \text{ cm}$, the hydrogen column density $N_{\text{H}} = 10^{23} \text{ cm}^{-2}$, a radio-quiet incident AGN SED, solar abundance $Z = Z_{\odot}$, a total cloud covering factor $\text{CF} = 50\%$, and a cloud distribution as a function of radius and volume density $f(r) \propto r^{\Gamma}$ with $\Gamma = -1.1$ and $g(n) \propto n^{\beta}$ with $\beta = -1$. We justify these parameters in detail in the following sections.

3.1. Responses of H α , H β , and Mg II to Continuum Variations

Following previous works in a spherically symmetric geometry (Korista & Goad 2000, 2004), we assume that the density of the clouds covers a broad range of $7 \leq \log n(\text{H}) [\text{cm}^{-3}] \leq 14$ with 0.125 dex spacing. The upper limit is subject to model uncertainties (Ferland et al. 2013), and the lower limit is determined by the absence of forbidden lines in the BLR. An ionizing flux range of $17 \leq \log \Phi(\text{H}) [\text{cm}^{-2} \text{ s}^{-1}] \leq 24$ with 0.125 dex spacing is chosen. The lower limit is related to the sublimation temperature ($\sim 1500 \text{ K}$) of dust grains, which corresponds to a hydrogen-ionizing flux of $\Phi(\text{H}) \sim 10^{17-18} \text{ cm}^{-2} \text{ s}^{-1}$ (Nenkova et al. 2008). The upper limit is unimportant since the emissivity for most lines is low at large $\Phi(\text{H})$. The ionization parameter is defined as the ratio of hydrogen-ionizing photon $Q(\text{H})$ to total hydrogen density $n(\text{H})$:

$$U_{\text{H}} \equiv \frac{Q(\text{H})}{4\pi R^2 n(\text{H})c} \equiv \frac{\Phi(\text{H})}{n(\text{H})c}, \quad (4)$$

⁹ $\log Q(\text{H}) = \log L_{\text{bol}} + A$, where A is about 9.8 (Arav et al. 2013), and $\log L_{\text{bol}} = \log \text{BC}_{3000\text{\AA}} + \log L_{3000\text{\AA}}$, where $\log \text{BC}_{3000\text{\AA}} = 0.71$ is the bolometric correction at 3000 Å using the average quasar SED from Richards et al. (2006).

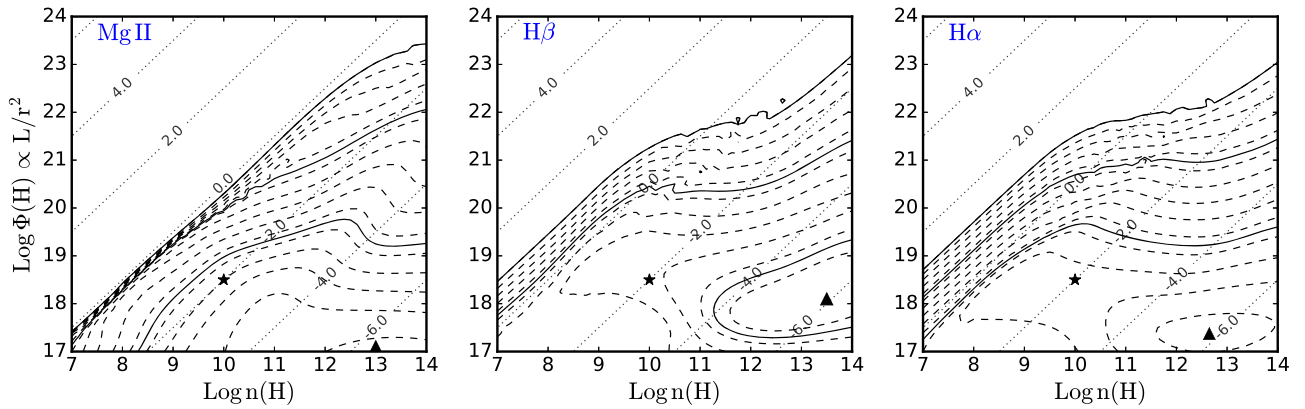


Figure 2. Contours of log EW for three emission lines as a function of the hydrogen density $n(\text{H})$ [cm^{-3}] and surface flux of hydrogen-ionizing photons $\Phi \propto L/r^2$. We assume the typical hydrogen column density $n(\text{H}) = 10^{23} \text{ cm}^{-2}$ and solar abundance (Z_{\odot}). The line EW is referenced to the incident continuum at 1215 \AA for direct comparisons with earlier work, which is directly proportional to the continuum reprocessing efficiency. The smallest decade contour (outermost) corresponds to 1 \AA , and each solid line is 1 decade, and dashed lines represent 0.125 decade steps. The dotted diagonal lines are photoionization parameters decreasing from the upper left ($\log U = 6$) to the lower right ($\log U = -6$). The triangles and stars are the EW peaks and the BLR parameters used in Davidson & Netzer (1979), respectively.

where R is the distance between the central ionizing source and the illuminated surface of the cloud, c is the speed of light, and $\Phi(\text{H})$ is the flux of ionizing photons. Constant U_{H} values are thus diagonal lines in the density–flux plane of Figure 2 (in log-log scale) ranging from 6 (upper left) to -6 (lower right). For each cloud (represented by a point in the density–flux plane), we assume a hydrogen column density $N_{\text{H}} = 10^{23} \text{ cm}^{-2}$, abundance $Z = Z_{\odot}$, and the same radio-quiet AGN SED (Mathews & Ferland 1987) to perform the photoionization calculations using CLOUDY (version 17.01, Ferland et al. 2017). In addition, we assume an overall covering factor of $\text{CF} = 50\%$, as adopted in Korista et al. (2004). Note that the incident continuum does not include the reprocessed emission from other clouds, nor do we consider the effects of cloud–cloud shadowing or continuum/line beaming.

We obtain the photoionization results on a grid of the density–flux plane, which include 3249 model calculations in Figure 2, where the contour represents the line equivalent width (EW, with respect to the incident continuum at 1215 \AA , for direct comparisons with earlier photoionization work) starting from $\text{EW} = 1 \text{ \AA}$ in the upper left to $\sim 1000 \text{ \AA}$ in the lower right. The EW is directly proportional to the continuum reprocessing efficiency for each line (see Figure 4 in Korista et al. 2004). For constant flux, the vertical y-axis in Figure 2 is equivalent to the radius axis. For all three lines, the most efficiently emitting regions are located in the lower right half, whereas the upper left half are regions of Comptonization (the clouds are transparent to the incident continuum). The EW peaks are marked by black triangles, while the stars correspond to the old standard BLR parameters (Davidson & Netzer 1979). The peak locations are determined by atomic physics and radiative transfer within the large range of line-emitting clouds. We can see that qualitatively the most efficient Mg II-emitting clouds are slightly more distant than those for the Balmer lines given $\Phi(\text{H}) \propto L_{\text{ion}}/r^2$ (hereafter L/r^2).

Next, we compute the overall line luminosity by summing over all grid points with proper weights determined from assumed distribution functions. Following Baldwin et al. (1995), the observed emission-line luminosity is the integration

given by

$$L_{\text{line}} \propto \int \int_{R_{\text{in}}}^{R_{\text{out}}} r^2 F(r) f(r) g(n) dn dr, \quad (5)$$

where $F(r)$ is the emission-line flux of a single cloud at radius r , and $f(r)$ and $g(n)$ are the assumed cloud covering fractions as functions of distance from the center and gas density, respectively.

We sum the grid emissivity in Figure 2 along the density axis at each radius to obtain the radial distribution of surface emissivity for different lines, as shown in the left panel of Figure 3. We note that only the density range of $8 \leq \log n(\text{H})$ (cm^{-3}) ≤ 12 is considered, since below $n(\text{H}) = 10^8 \text{ cm}^{-3}$ the clouds are inefficient in producing emission lines and above $n(\text{H}) = 10^{12} \text{ cm}^{-3}$ the clouds mostly produce thermalized continuum emission rather than emission lines (Korista & Goad 2000). In addition, we only sum the contributions from ionized clouds with $6 \leq \log U_{\text{H}} \leq 11.25$ (see details in Korista & Goad 2000; Korista et al. 2004; Korista & Goad 2019).

In the left panel of Figure 3, we also consider the case where the continuum luminosity at 3000 \AA of the quasar drops by a factor of 10, i.e., $L_{3000 \text{ \AA}}$ decreases from 10^{45} to $10^{44} \text{ erg s}^{-1}$ (gray shaded area in Figure 4), corresponding to $Q(\text{H}) \simeq [10^{55.5}, 10^{54.5}]$ (s^{-1}). When the quasar continuum changes from the bright state (solid lines) to the faint state (lighter lines) by 1 dex, the radial emissivity function simply shifts to the left by 0.5 dex (since $\Phi(\text{H}) \propto L/r^2$) assuming no dynamical structure changes of the BLR, as well as its inner and outer boundaries. Mg II emissivity changes much less than Balmer lines in our assumed BLR, and this difference in the level of line emissivity changes from the bright state to the faint state increases with increasing radius.

Following previous works (e.g., Goad et al. 1993; Korista et al. 2004), we define a responsivity parameter

$$\eta = \frac{d \log F(r)}{d \log \Phi(\text{H})} \propto -0.5 \frac{d \log F(r)}{d \log r}, \quad \text{since } \Phi(\text{H}) \propto r^{-2}, \quad (6)$$

to describe the efficiency of converting the change in the ionizing continuum flux to the change in the responding line flux. Integrating over the full line-emitting region, we have the

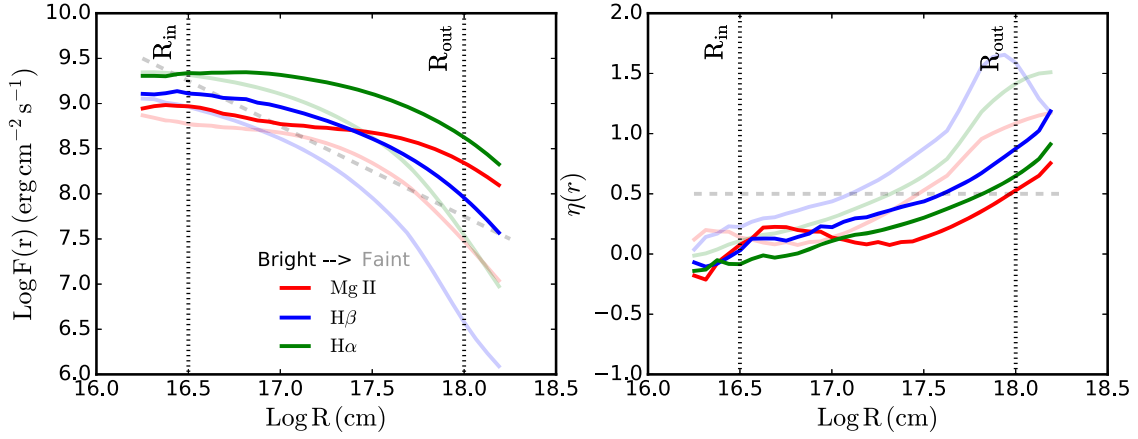


Figure 3. Left: radial emissivity function. Emission-line radial surface fluxes are based on the weighting function along the gas density axis. Right: radial responsivity function. η is calculated based on Equation (6). The gray dashed line of $F(r) \propto r^{-1}$ (left) indicates $\eta = 0.5$ (right). The radial distance is calculated from the continuum luminosity $L_{3000 \text{ \AA}} = [44, 45] \text{ erg s}^{-1}$ (transparent and solid). The vertical dashed lines mark inner and outer boundaries of the BLR ($R_{\text{in}} \simeq 12 \text{ lt-day}$, $R_{\text{out}} \simeq 385 \text{ lt-day}$).

relation $L_{\text{line}} \propto L_{\text{con}}^{\eta}$. Furthermore, if we assume $F(r) \propto r^{\gamma}$ with $\gamma = -1$, then $\eta = -\gamma/2 = 0.5$, which is a rough approximation for several UV/optical emission lines (e.g., Goad et al. 2012; see also the dashed gray lines in Figure 3).

The right panel of Figure 3 shows that the responsivities η of Balmer lines and Mg II are correlated with the emitting radius and anticorrelated with the incident luminosity $L(t)$ at different times. Since the clouds with $\eta(r, L(t)) > 1$ and < 0 will not respond appropriately to the variations in the ionizing continuum (Korista et al. 2004), we generally consider the $0 < \eta < 1$ region. Since η starts to exceed 0 at $R = 10^{16.5} \text{ cm}$ for both the bright and faint states, we adopt $R_{\text{in}} = 10^{16.5} \text{ cm}$ (12 lt-day) for our LOC model. As long as the inner boundary is small, it has a minor impact on our results because the clouds there have very high density ($> 10^{12} \text{ cm}^{-3}$) and low responsivity η , with cloud emission dominated by continuum and not emission lines. However, the outer BLR boundary is important in our LOC model, which will determine the “breathing” of the broad emission lines (see Section 3.2). Note that although η will be larger than 1 at $R_{\text{out}} = 10^{18} \text{ cm}$ in the faint state, most of these clouds are emitting inefficiently and will have little impact on our results.

To calculate the line luminosity, we still need to specify the distribution functions of clouds, i.e., $f(r)$ and $g(n)$. Traditionally LOC models have used empirical parameterizations for these distribution functions aiming at reproducing the observed emission-line properties. For example, according to Baldwin et al. (1995), $f(r) \propto r^{\Gamma}$ and $g(n) \propto n^{\beta}$ ($\Gamma = -1$ and $\beta = -1$) are simple and reasonable assumptions for BLR clouds. This parameterization of $f(r)$ and $g(n)$ results in equal weighting for each grid point in the density–flux plane in log scale. For the best-known NGC 5548, Korista & Goad (2000) suggested that $-1.4 < \Gamma < -1$ is the optimized range to recover the observed time-averaged UV spectrum in 1993, and hence it was fixed to -1.2 in Korista & Goad (2019). In this work we fix $\Gamma = -1.1$ to match the Mg II luminosity observed in a rare Mg II changing-look quasar (CLQ; see the details in Section 4.2). Hence, Equation (5) becomes

$$L_{\text{line}} \propto \int d(\log n) \int_{R_{\text{in}}}^{R_{\text{out}}} r^{1.9} F(r) d(\log r). \quad (7)$$

Given the luminosity range of the quasar, we obtain the LOC predicted $L_{\text{con}}-L_{\text{line}}$ relation in Figure 4. In the left panel, Mg II varies at a slower rate with continuum than the Balmer lines, particularly in the gray region that encloses the typical luminosity range of a CLQ (e.g., MacLeod et al. 2016; Yang et al. 2018). In this shaded region, when the continuum luminosity drops by 1 dex, the Mg II luminosity is only reduced by 0.45 dex, which is less than the luminosity reduction in Balmer lines (e.g., 0.6 dex for $H\alpha$ and 0.7 dex for $H\beta$). In the right panel, we show different line ratios as a function of continuum luminosity. With decreasing central luminosity, the ratios of $H\alpha/H\beta$ and Mg II/ $H\beta$ increase, which is consistent with the theoretical results in Baldwin et al. (1995) and observations of the quasar composite spectrum (Vanden Berk et al. 2001) and CLQs (MacLeod et al. 2016, 2019; Yang et al. 2018).

3.2. Reproducing the “Breathing” of Broad Lines

Given the long dynamical timescale (more than a few decades) in the dust sublimation region, the physical outer boundary of the BLR is determined by the average luminosity state at least decades ago and could be largely unrelated to the current luminosity state. Here we explore the possibility that R_{out} deviates from that estimated based on the current luminosity and the consequences on the breathing behaviors of different broad lines.

If we consider that the previous $L_{3000 \text{ \AA}}$ that set the outer BLR boundary is 10 times smaller or larger than the current average luminosity, we obtain $R_{\text{out}} = 10^{17.5}$ or $10^{18.5} \text{ cm}$ assuming $\log \Phi(\text{H}) = 17.9 \text{ cm}^{-2} \text{ s}^{-1}$ and that the BLR outer boundary has not yet had enough time to dynamically adjust itself owing to luminosity state changes. Thus, with three values of $R_{\text{out}} = 10^{17.5}, 10^{18}$, and $10^{18.5}$, we produce three cases that have different behaviors in the relation between line width and luminosity (e.g., second and third rows of Figure 5): in the left column, $H\beta$ shows “breathing,” but Mg II and $H\alpha$ only cover half of the luminosity range (partially breathing); in the middle column, none of the lines show “breathing” (no-breathing); and in the right column, all three lines show “breathing” (see details below).

The resulting radial distributions of line emission are presented in the top panels of Figure 5. Similarly, we consider

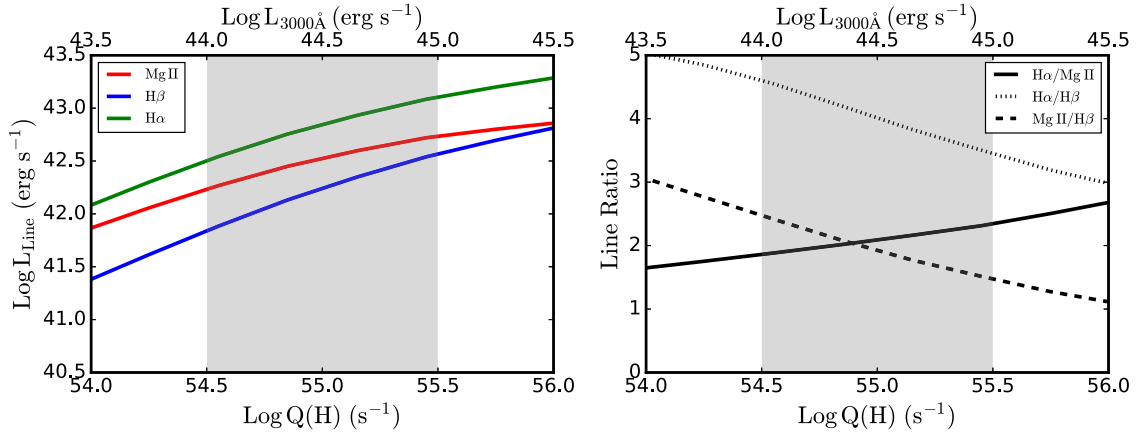


Figure 4. Left: responses of line luminosity to continuum changes in the fiducial LOC model. The line luminosity is computed assuming a global covering fraction of $C_f = 50\%$, i.e., half of the continuum emission is covered by the clouds. Right: line ratios as a function of continuum luminosity in the fiducial LOC model. The gray shaded regions enclose a factor of 10 change in continuum luminosity to mimic a CLQ (or extreme variability quasar).

a continuum change of 1 dex from the bright state (solid lines) to the faint state (lighter lines) to mimic a CLQ. These radial emissivity profiles will not only shift to the left but also move down owing to $\Phi(H) \propto L/r^2$. The Mg II emissivity peak is always located at larger radii than those for the Balmer lines. Moreover, the Mg II and H α emissivity profiles are more narrowly distributed than that of H β . In the left column, the maximum emissivity for all three lines is located very close to the outer boundary of the BLR in the bright state. In the faint state, the maximum emissivity of H β is shifted to inside the outer boundary, while the maximum emissivities of Mg II and H α are still near the outer boundary.

Assuming that the BLR is virialized,¹⁰ we compute the average virial velocity and the corresponding observed broad-line width (line dispersion for both σ_{peak} and σ_{eff}) for each line and display the results in the bottom panels of Figure 5. The σ_{peak} is calculated based on the peak-emissivity radius R_{peak} . This simplification is adopted to demonstrate the concept of different “breathing” modes since the line emission is nearly dominated by the emissivity peak (Baldwin et al. 1995). We also consider a more realistic line width estimation, the effective line width σ_{eff} weighted by the radial line emissivity:

$$\sigma_{\text{eff}} = \frac{\int \sigma r^{1.9} F(r) d \log(r)}{\int r^{1.9} F(r) d \log(r)}, \quad (8)$$

where $\sigma = \sqrt{\frac{M_{\text{BH}} G}{R_f}}$, $M_{\text{BH}} = 10^{8.5} M_{\odot}$, and $f = 4.47$.

As shown in Figure 3, the σ_{peak} -based cases clearly present distinctions between breathing and no-breathing regions, and hence we use it to define three breathing categories. However, for more realistic situations, all σ_{eff} -based cases show identical anticorrelations, but only with different slopes more skewing toward breathing or no-breathing scenarios. Both estimations demonstrate that Mg II is always the least breathing among the three lines for $R_{\text{out}} = 10^{18}$ cm. Comparing to the typical observed line width ($\sigma \sim 1700 \text{ km s}^{-1}$) for H β in SDSS quasars with $M_{\text{BH}} = 10^{8.5} M_{\odot}$, σ_{eff} ($\sim 1600 \text{ km s}^{-1}$) is preferred over the use of σ_{peak} ($\sim 1000 \text{ km s}^{-1}$). In addition, since the left column is the most consistent with observed properties for the Balmer

lines and Mg II (e.g., Park et al. 2012; Shen 2013; Yang et al. 2019), we will use the σ_{eff} -based partially breathing model as our fiducial model to produce further relations and CL sequence in Sections 3.3 and 4.2. This model is the same fiducial LOC model for all other predictions.

3.3. The Relation between Broad-line Width and Equivalent Width

The intrinsic Baldwin effect (BE; Baldwin 1977) states that the line EW decreases with increasing continuum luminosity for a given quasar. From Equation (6),

$$\eta = \frac{d \log F(r)}{d \log \Phi(H)} = \frac{d \log \text{EW}}{d \log \Phi(H)} + 1, \quad (9)$$

and therefore $L_{\text{con}} \propto \text{EW}^{\eta-1}$, which means that the slope of the intrinsic BE is governed by the responsivity η that varies with the continuum luminosity and the formation radius. For instance, the responsivity η for H β in partially breathing BLRs for the bright (faint) state is ~ 0.5 (0.7) at the most effective formation radius $R_{\text{eff}} = 10^{17.52}$ ($10^{17.25}$) cm (see Figures 4 and 9). Thus, the BE slope varies between -0.5 and -0.3 from the bright to the faint states, which is consistent with the prediction (~ -0.4) in Figure 6. For the well-studied AGN NGC 5548, the intrinsic BE slope ~ -0.6 predicted by LOC models has been confirmed by observations (e.g., Gilbert & Peterson 2003; Rakić et al. 2017), verifying the reliability of the LOC model. In addition, the average EW values of different emission lines (i.e., $\log \text{EW}_{\text{MgII}} = 1.5$ and $\log \text{EW}_{\text{H}\beta} = 1.8$) in Figure 6 are also consistent with observed values for SDSS quasars around $L_{3000 \text{ \AA}} = 10^{44.5} \text{ erg s}^{-1}$ (Shen et al. 2011). Note that the EWs for H β and H α are computed using $L_{5100 \text{ \AA}}$, scaled from $L_{3000 \text{ \AA}}$ by a factor of 1.8 based on the average quasar SED (Richards et al. 2006).

On the other hand, the model also predicts a correlation between the line width and the EW. This correlation is driven by the combined effect of breathing and the BE: both line width and EW are anticorrelated with continuum luminosity. However, if Mg II is partially breathing in the luminosity range probed in Figure 6, it predicts a steeper slope of ~ 4 for Mg II in logarithm space than the observed slope (~ 1) in population studies (Dong et al. 2009; Shen et al. 2011). It is likely that the

¹⁰ Note that we do not have enough information to reconstruct the detailed kinematic structure of the BLR. It is possible that some portion of the BLR gas is not in a virialized component, which could contribute to the wings of the broad lines (e.g., Ho et al. 2012; Popović et al. 2019).

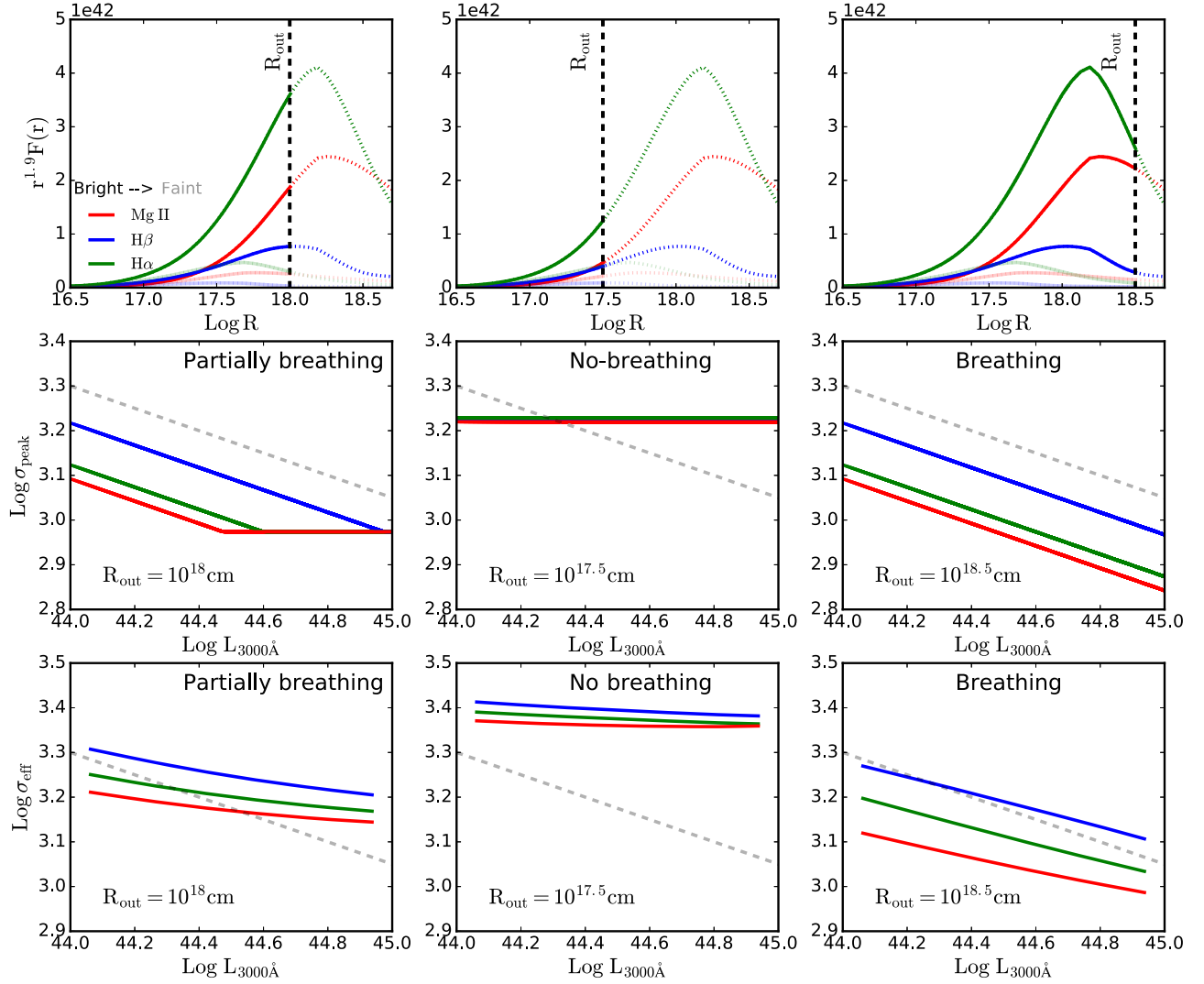


Figure 5. Radial emissivity functions for different lines (top panels) and the corresponding (σ_{peak} -based and σ_{eff} -based) breathing modes (middle and lower panels). In the top panels, the dotted line corresponds to the bright state, and the lighter line corresponds to the faint state with a factor of 10 (1 dex) drop in flux. For the faint state, the line emissivity peaks move to the lower left accordingly. The dashed vertical line marks the outer radius of the BLR, and the dotted portions of the emissivity profile are not used in the calculation of line luminosity. Each column corresponds to a different outer radius R_{out} to demonstrate the resulting luminosity–line width (L – σ) relation. Perfect breathing corresponds to $L \propto R^2 \propto \sigma^{-4}$ (dashed gray lines).

relations revealed here for a single quasar (i.e., the relation is intrinsic) contribute to the global relation observed for populations of quasars with different BH masses and luminosities.

4. Implications

The appeal and caveats of the LOC model have been discussed extensively in earlier work (e.g., Korista & Goad 2000, 2004). While the LOC model is quite successful in reproducing the bulk of the observed properties of the broad-line emission, we fully acknowledge the empirical nature of this approach. For example, the modeling of the covering factors (weights) as functions of radius and cloud density is somewhat ad hoc. Nevertheless, we found that this empirical photoionization model can explain most of the observed variability properties of the Mg II line and their differences from those for the Balmer lines.

Assuming that our fiducial LOC models are the correct prescription for broad-line emission in quasars, we discuss the

implications of the predicted broad-line variability, with an emphasis on the Mg II line.

4.1. Mg II Reverberation Mapping

As discussed in Section 1, Mg II is an important broad line of RM interest at intermediate redshifts with optical spectroscopy. Confirming earlier photoionization calculations (e.g., Korista & Goad 2000; Korista et al. 2004), we found that the variability properties of broad Mg II can be reasonably well explained by the LOC model. First, the broad Mg II responds to the continuum variability at a lower level than the broad Balmer lines, which means that the Mg II lags will be more difficult to detect in general. The fact that the Mg II gas on average is located at slightly larger distance than the Balmer line gas also adds to the difficulty of detecting Mg II lags, since longer monitoring duration is required to capture the lag. Moreover, there is a general mismatch between the formation radius of the lines and the characteristic timescale of the driving continuum, which means that in general the measured delays, and thus

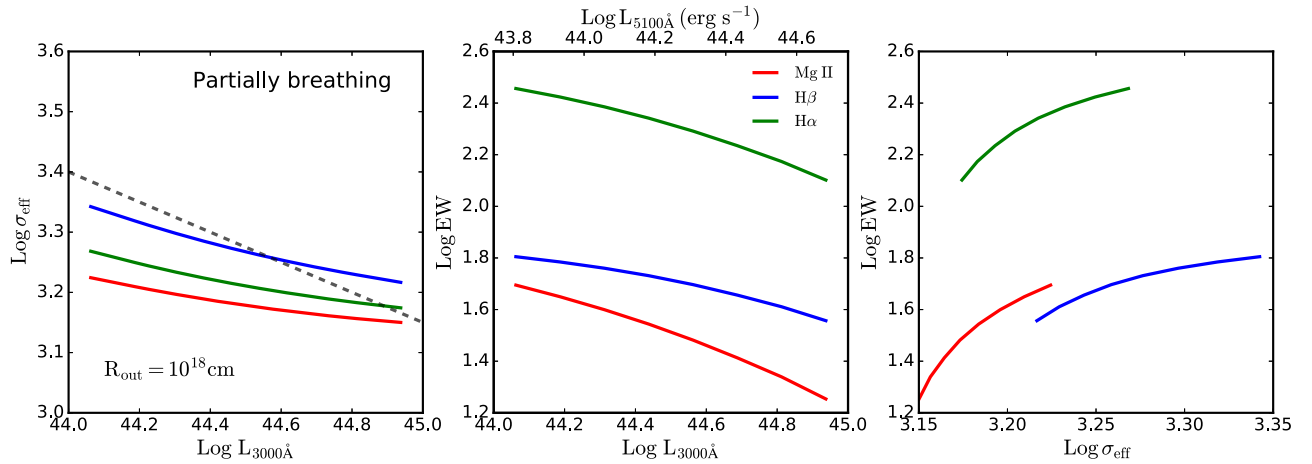


Figure 6. Relations among $L_{3000\text{\AA}}$, EW, and σ_{eff} . The calculation is based on our fiducial partially breathing mode assuming $R_{\text{out}} = 10^{18}$ cm. The dashed gray line in the left panel indicates the perfect breathing model. The EW of H β and H α is computed with the continuum flux at 5100 \AA .

inferred “sizes,” are underestimated (Perez et al. 1992; Goad & Korista 2014).

Perhaps a more striking feature of Mg II variability is the general lack of breathing when luminosity changes. We have argued that this lack of breathing could be explained by the possibility that the Mg II gas with maximum emission efficiency is near the outer physical boundary of the BLR, and hence the flux-weighted radius of the Mg II-emitting clouds does not vary much with luminosity.¹¹ Alternatively, if the inner and outer boundaries of the BLR are fixed and $\eta(r, L(t))$ is constant over radius, which means that the responsivity η is the same for the line core and wings, the line will not display breathing, as the entire profile scales up and down with continuum variation (e.g., Korista & Goad 2004). A third possibility is that if the outer part of the BLR is dominated by turbulent motion (or nonvirial motion), the line width of Mg II will also be less sensitive to continuum variations (e.g., Goad et al. 2012). The lack of breathing for Mg II suggests that there is no intrinsic $R-L$ relation for the Mg II BLR. However, a global $R-L$ relation may still exist for quasars over a broad BH mass and luminosity range, if the outer radius R_{out} scales with BH mass. Figure 7 demonstrates the possible existence of a global $R-L$ relation and the absence of an intrinsic $R-L$ relation for Mg II. More RM results on Mg II will be important to test the existence, or lack thereof, of a global $R-L$ relation (e.g., Shen et al. 2015, 2016; Czerny et al. 2019).

One assumption in our photoionization modeling is that the physical BLR structure does not change over the period of the continuum variability. It is possible that R_{out} will slowly change on dynamical timescale at this radius ($>10^2$ yr for our default parameters of $M_{\text{BH}} = 10^{8.5} M_{\odot}$ and $R_{\text{out}} \sim 0.3$ pc) and may eventually settle down at a different value in a new average luminosity state over the much longer lifetime of the quasar. This possibility could also be responsible for a global $R-L$ relation for Mg II.

4.2. A Changing-look Sequence

Our LOC models also have implications for the behaviors of broad-line responses to continuum changes in the population of

$R-L$ relation :

Individual: MgII H β

Global

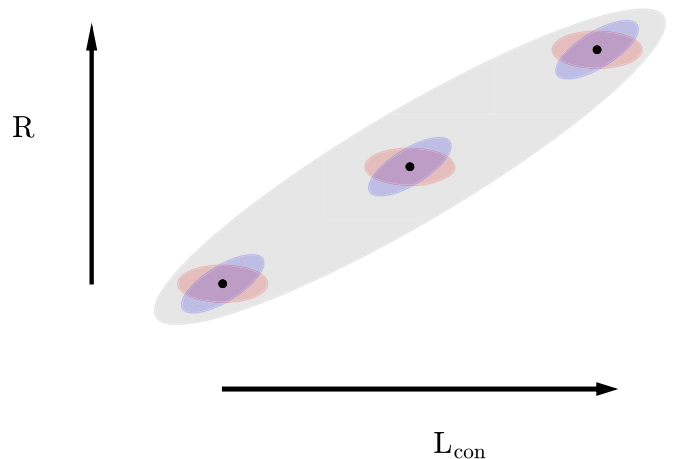


Figure 7. Cartoon for the $R-L$ relation. The gray ellipse represents a global $R-L$ relation for the population of quasars with different BH masses and luminosities. The small blue and red ellipses represent the intrinsic $R-L$ relation for a single quasar with variable luminosity, for H β and Mg II, respectively. The “breathing” mode for H β in individual quasars is the result of the intrinsic $R-L$ relation. For Mg II there is no intrinsic $R-L$ relation, which results in no “breathing” mode for Mg II.

optically identified CLQs, or more generally, extreme variability (or hypervariable) quasars (e.g., Rumbaugh et al. 2018).

Most of the CLQs reported so far are spectroscopically defined by dramatic changes in the broad Balmer line flux between the bright and the dim states (e.g., LaMassa et al. 2015; MacLeod et al. 2016, 2019; Runnoe et al. 2016; Sheng et al. 2017; Yang et al. 2018). In most, if not all, of these cases, broad Mg II remains visible even in the dim state (e.g., MacLeod et al. 2019; Yang et al. 2019).

With our LOC models, we can qualitatively explain the persistence of broad Mg II in a CL event. Figure 8 presents a time sequence of synthetic spectra with the continuum luminosity decreasing from 10^{45} to 10^{43} erg s^{-1} , for the fiducial model ($R_{\text{out}} = 10^{18}$ cm) that can reproduce the observed Mg II variability properties (see Sections 3.1 and 3.2). Each spectrum

¹¹ Under different model parameters, Mg II can also exhibit breathing (Figure 5), as observed in rare cases (Dexter et al. 2019).

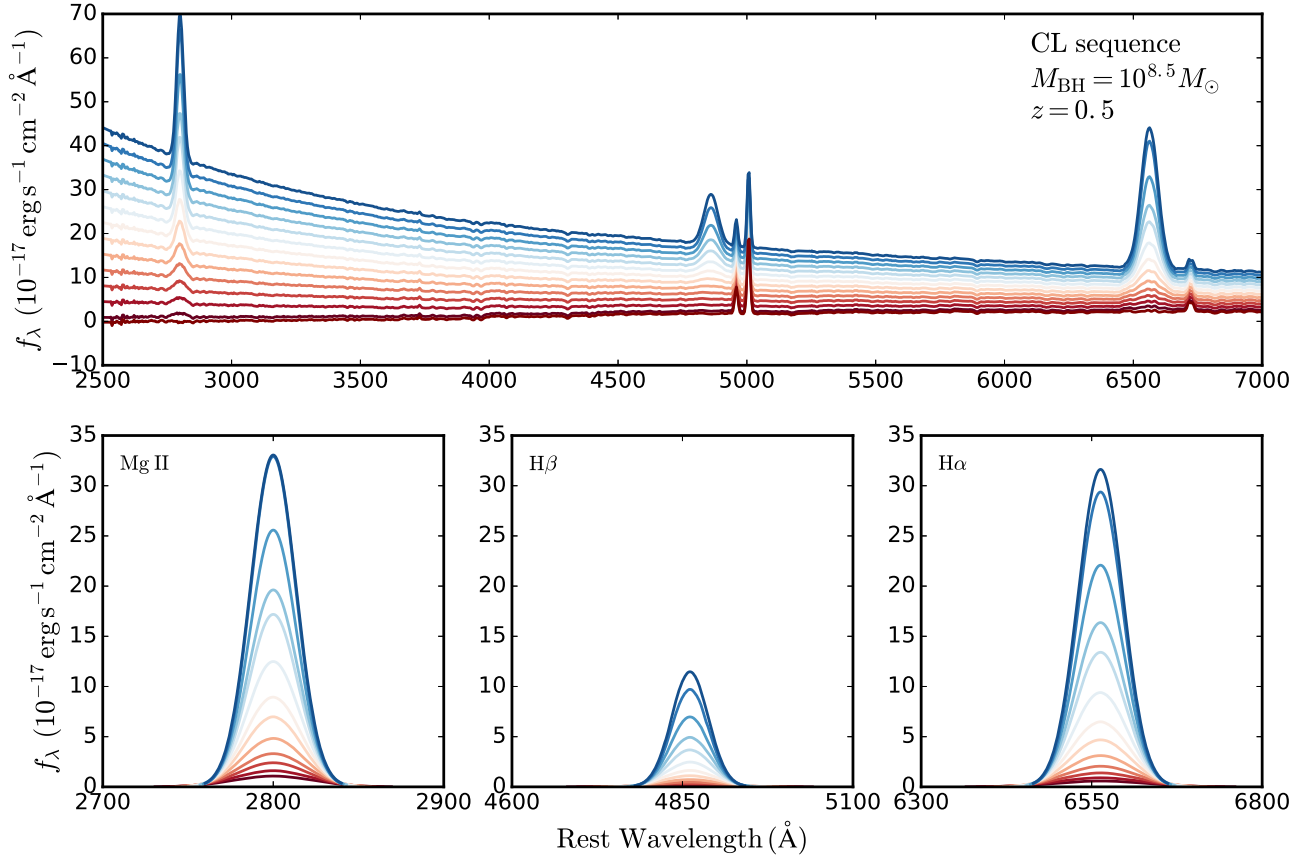


Figure 8. CL sequence for quasars. Bottom panels: theoretical line profiles of Mg II, H β , and H α predicted by the fiducial LOC model assuming a quasar with $M_{\text{bh}} = 10^{8.5} M_{\odot}$ at $z = 0.5$. The line flux and width are governed by the $L_{\text{line}}-L_{\text{con}}$ and $L_{\text{con}}-\sigma$ relations in Figure 4 and the partially breathing case in Figure 5. All three lines are simulated by single Gaussians. Top panel: $L_{3000 \text{ \AA}}$ is reduced from 10^{45} to $10^{43} \text{ erg s}^{-1}$ for the full spectrum in steps of 0.15 dex. Each spectrum consists of a power-law continuum, a host galaxy template, and Gaussians of broad and narrow lines except for the faintest epoch, which only contains host emission and narrow lines. The second-faintest epoch has an Mg II luminosity tuned to $\sim 10^{41.5} \text{ erg s}^{-1}$ with $\Gamma = -1.1$, which is consistent with the observed line luminosity in the Mg II CLQ reported in Guo et al. (2019). In each panel, the color gradient represents luminosity changes from the brightest epoch (blue) to the faintest epoch (red).

consists of a quasar power-law continuum, a host galaxy component,¹² and broad/narrow emission lines (e.g., H α , H β , Mg II, [O III], and [S II]) described by single-Gaussian functions. In the faintest state we only include the host galaxy and narrow emission lines. We adopt a quasar continuum power-law slope $\alpha = -1.56$ ($f_{\lambda} = \lambda^{\alpha}$; e.g., Vanden Berk et al. 2001). We start at the brightest epoch with $L_{3000 \text{ \AA}} = 10^{45} \text{ erg s}^{-1}$ and reduce the continuum luminosity in steps of 0.15 dex. The strengths of the broad emission lines are computed from our fiducial LOC model at each continuum luminosity. Note that the index Γ for the radial distribution of cloud coverage determines the line luminosity and the BH mass governs the line dispersion (since the effective radius is determined from photoionization). For our fiducial LOC model, the M_{BH} is fixed to $10^{8.5} M_{\odot}$, which yields $\sigma_{\text{eff}} = 10^{3.4} \text{ km s}^{-1}$ at continuum luminosity of $10^{43} \text{ erg s}^{-1}$. Meanwhile, Mg II luminosity is required to be $\sim 10^{41.5} \text{ erg s}^{-1}$ at this continuum luminosity to match the only reported Mg II CLQ in Guo et al. (2019), which led to the choice of $\Gamma = -1.1$ in Section 2 for our fiducial LOC model.

From the sequence in Figure 8, it is obvious that when the broad Balmer lines almost disappear (e.g., become undetectable), the broad Mg II emission remains visible. When the continuum luminosity continues to drop, broad Mg II will

eventually become too weak to be detectable. Indeed, we have found an example of an Mg II CL object from a systematic search with repeated SDSS spectra (Guo et al. 2019). In that case, the Mg II equivalent width dramatically changed from $\sim 100 \text{ \AA}$ to being consistent with zero, with little continuum change due to the dominance of the host light at the dim state. In Figure 9, we calculate the σ_{eff} -based average radius for each epoch in this CL sequence, which decreases when luminosity decreases. Most importantly, the average radius (line width) of Mg II decreases (increases) more slowly than those of the Balmer lines, verifying our fiducial model in Figures 5 and 6.

We note that there is currently some ambiguity in the observational definition of ‘‘CLQs’’ based on the appearances of the broad Balmer lines, i.e., the detection of broad Balmer lines is dependent on signal-to-noise ratio. Our LOC calculations demonstrate that the variability of the broad emission lines in a CLQ can be fully explained by photoionization responses to the dramatic continuum changes. There is nothing special about the properties of the broad emission lines in CLQs compared to normal quasars, except for their extreme continuum variability. For these reasons, ‘‘extreme variability quasars,’’ or ‘‘hypervariable quasars,’’ is a more appropriate category term for these objects in our opinion.

Given the sequence of broad-line spectra shown in Figure 8 following the fading of continuum emission, it is possible to catch the quasar in a state where there is detectable broad Mg II but no detectable broad Balmer lines. Roig et al. (2014)

¹² The host galaxy template is taken from the actual spectrum of a recently discovered Mg II changing-look object (Guo et al. 2019).

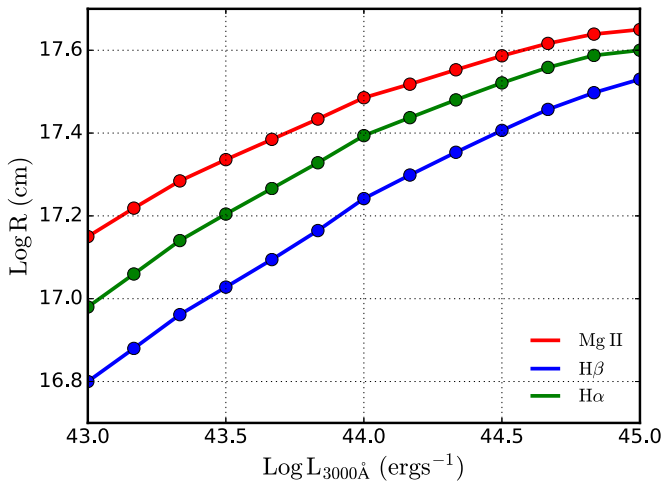


Figure 9. Average line-emitting radius for each epoch in the CL sequence shown in Figure 8, estimated using the emissivity-weighted line width σ_{eff} . The average radius of Mg II decreases more slowly than the Balmer lines.

discovered that there is a rare population of broad Mg II emitters in spectroscopically confirmed massive galaxies from the SDSS. We postulate that these broad Mg II emitters may be the transition quasar population where the quasar continuum and broad Balmer line flux had recently dropped by a large factor but the broad Mg II flux is still detectable on top of the stellar continuum. Using the sample of broad Mg II emitters from Roig et al. (2014), we confirmed that the EWs of the broad Mg II follow the extrapolated Baldwin effect in our LOC model to the lower luminosity range¹³ of $L_{3000} \sim 10^{43}$ erg s $^{-1}$. Thus, the LOC model provides a natural explanation for these rare broad Mg II emitters in otherwise normal galaxy spectra.

4.3. Comparison with a Well-studied Case: NGC 5548

NGC 5548 is the ideal case to compare with our LOC model predictions given its extensive optical/UV RM data in the past several decades. We collected the published RM results from the 13 yr AGN Watch project (Peterson et al. 2004) and the six-month Space Telescope and Optical Reverberation Mapping (AGN STORM) project (Pei et al. 2017) to investigate the relations between continuum and emission-line fluxes (i.e., H β). Unfortunately, for NGC 5548 the data on Mg II are much less than the data on H β , and therefore we do not consider Mg II here.

As shown in Figure 10, the continuum flux (host corrected) at 5100 Å and line flux are well correlated over several decades (see also Goad & Korista 2014). The time lags (or emitting size) between the continuum and H β display the expected breathing during the AGN Watch program (e.g., Gilbert & Peterson 2003; Goad et al. 2004; Cackett & Horne 2006). At the end of AGN Watch around 2000, NGC 5548 was in a historic low state for some considerable time before returning to the average historic luminosity in the more recent AGN STORM campaign. If the outer BLR boundary was set during the low state around 2000, we would expect the 2014 AGN STORM RM results to have weaker H β strength and a reduced lag (since the BLR had been physically truncated), consistent with the results around 2000 (from AGN Watch) and in 2014

¹³ We found that the 3000 Å luminosities for these broad Mg II emitters were underestimated by an erroneous factor of 100 in the original Roig et al. paper (B. Roig 2019, private communications).

(STORM). Therefore, it is plausible that there is a physical outer boundary of the BLR set by the prior average luminosity state, as postulated in our model.

5. Conclusions

In this work we have studied the variability of broad Mg II, H α , and H β in the framework of photoionization of BLR clouds by the ionizing continuum from the accretion disk in quasars. We adopt the popular but empirical LOC model with typical parameters used in the literature to qualitatively reproduce the observed variability properties of the three low-ionization broad lines.

Our main findings are as follows:

1. The LOC model confirms that the emissivity-weighted radius decreases in the order of Mg II, H α , and H β (Figures 2 and 5), which is consistent with limited RM results where more than one line has detected lags (Clavel et al. 1991; Peterson & Wandel 1999; Shen et al. 2016; Grier et al. 2017) and previous photoionization predictions from Goad et al. (1993), Korista & Goad (2000), and Korista et al. (2004). It also predicts that the H β -emitting gas is more broadly distributed radially than Mg II and H α (Figure 5).
2. The observed weaker variability and slower response of Mg II compared to the Balmer lines are recovered over a broad range of quasar continuum variations (Figure 4), which is again consistent with previous studies (e.g., Goad et al. 1993; Korista & Goad 2000). These results come naturally from photoionization calculations that capture various excitation mechanisms and radiative transfer effects. Variability dilution due to the larger average distance of Mg II gas likely also contributes to this difference between Mg II and Balmer line variability.
3. The general lack of “breathing” of the broad Mg II line can be explained by the possibility that the most efficient Mg II-emitting clouds are always near the outer physical boundary of the BLR. On the other hand, the Balmer line gas is inside this outer BLR boundary, and the average line formation radius shifts as continuum luminosity changes to produce the “breathing” effect (Figure 5). Under certain circumstances when the Mg II gas is also mostly inside the outer BLR boundary, Mg II can also display the “breathing” behavior.
4. Based on these photoionization calculations, there is a natural sequence of the successive weakening of H β , H α , and Mg II, when the ionizing continuum decreases. The “changing-look” behavior in CLQs can be fully explained by the photoionization responses of the broad emission lines to the extreme variability of the continuum, adding to mounting evidence that most CLQs are caused by intrinsic accretion rate changes. Our results provide natural explanations for the persistence of broad Mg II line in CLQs and broad Mg II emitters in otherwise normal galaxies.

The success of reproducing most of the observed Mg II variability properties, which only became available recently for statistical samples, with simple LOC models suggests that photoionization is the dominant process that determines the observed variability properties of the broad-line emission. Future more RM results on Mg II will further test the LOC photoionization model, and to confirm the existence of a global

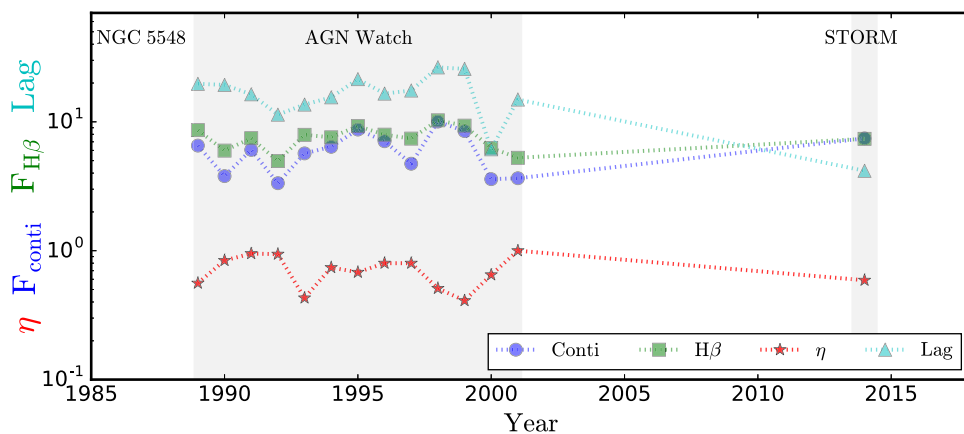


Figure 10. Time evolution of the continuum flux at 5100 Å in units of $10^{-15} \text{ cm}^{-2} \text{ s}^{-1} \text{ \AA}^{-1}$, broad H β flux in units of $10^{-13} \text{ ergs cm}^{-2} \text{ s}^{-1}$, H β time lag in units of days, and responsivity (η). The data from 1988–2001 and 2014 are taken from the AGN Watch (Peterson et al. 2004) and STORM (Pei et al. 2017) projects, respectively. The host contribution and narrow-line H β flux were removed when calculating the continuum and broad-line fluxes.

$R-L$ relation for Mg II, which is a prerequisite to using the Mg II line as a single-epoch virial BH mass estimator for quasars.

We thank the referee for a thorough report and many suggestions that greatly improved this work. We also thank B. Roig for useful discussions on broad Mg II emitters; Luis Ho, Jon Trump, and Gary Ferland for comments on the manuscript; and the CLOUDY team for valuable suggestions. Y.S. acknowledges support from an Alfred P. Sloan Research Fellowship and NSF grant AST-1715579. Z.H. is supported by NSFC-11903031 and USTC Research Funds of the Double First-Class Initiative YD 3440002001. T.W. is supported by NSFC-11833007. M.K. is supported by Astronomical Union Foundation under grant No. U1831126 and Natural Science Foundation of Hebei Province No. A2019205100.

ORCID iDs

Hengxiao Guo (郭恒潇) <https://orcid.org/0000-0001-8416-7059>
 Yue Shen <https://orcid.org/0000-0003-1659-7035>
 Zhicheng He <https://orcid.org/0000-0003-3667-1060>
 Tinggui Wang <https://orcid.org/0000-0002-1517-6792>
 Xin Liu <https://orcid.org/0000-0003-0049-5210>
 Mouyuan Sun <https://orcid.org/0000-0002-0771-2153>
 Qian Yang <https://orcid.org/0000-0002-6893-3742>
 Zhenfeng Sheng <https://orcid.org/0000-0001-6938-8670>

References

Arav, N., Borguet, B., Chamberlain, C., Edmonds, D., & Danforth, C. 2013, *MNRAS*, 436, 3286
 Baldwin, J., Ferland, G., Korista, K., & Verner, D. 1995, *ApJL*, 455, L119
 Baldwin, J. A. 1977, *ApJ*, 214, 679
 Barth, A. J., Bennert, V. N., Canalizo, G., et al. 2015, *ApJS*, 217, 26
 Bentz, M. C., & Katz, S. 2015, *PASP*, 127, 67
 Bentz, M. C., Peterson, B. M., Pogge, R. W., Vestergaard, M., & Onken, C. A. 2006, *ApJ*, 644, 133
 Blandford, R. D., & McKee, C. F. 1982, *ApJ*, 255, 419
 Cackett, E. M., Gültekin, K., Bentz, M. C., et al. 2015, *ApJ*, 810, 86
 Cackett, E. M., & Horne, K. 2006, *MNRAS*, 365, 1180
 Cai, Z.-Y., Wang, J.-X., Gu, W.-M., et al. 2016, *ApJ*, 826, 7
 Clavel, J., Reichert, G. A., Alloin, D., et al. 1991, *ApJ*, 366, 64
 Czerny, B., Olejak, A., Rałowski, M., et al. 2019, *ApJ*, 880, 46
 Davidson, K., & Netzer, H. 1979, *RvMP*, 51, 715

Denney, K. D., Peterson, B. M., Dietrich, M., Vestergaard, M., & Bentz, M. C. 2009, *ApJ*, 692, 246
 Dexter, J., & Agol, E. 2011, *ApJL*, 727, L24
 Dexter, J., Xin, S., Shen, Y., et al. 2019, *ApJ*, 885, 44
 Dong, X.-B., Wang, T.-G., Wang, J.-G., et al. 2009, *ApJL*, 703, L1
 Du, P., Lu, K.-X., Zhang, Z.-X., et al. 2016, *ApJ*, 825, 126
 Ferland, G. J., Chatzikos, M., Guzmán, F., et al. 2017, *RMxAA*, 53, 385
 Ferland, G. J., Porter, R. L., van Hoof, P. A. M., et al. 2013, *RMxAA*, 49, 137
 Gilbert, K. M., & Peterson, B. M. 2003, *ApJ*, 587, 123
 Goad, M. R., Koratkar, A. P., Axon, D. J., Korista, K. T., & O'Brien, P. T. 1999a, *ApJL*, 512, L95
 Goad, M. R., Koratkar, A. P., Kim-Quijano, J., et al. 1999b, *ApJ*, 524, 707
 Goad, M. R., & Korista, K. T. 2014, *MNRAS*, 444, 43
 Goad, M. R., Korista, K. T., & Knigge, C. 2004, *MNRAS*, 352, 277
 Goad, M. R., Korista, K. T., & Ruff, A. J. 2012, *MNRAS*, 426, 3086
 Goad, M. R., O'Brien, P. T., & Gondhalekar, P. M. 1993, *MNRAS*, 263, 149
 Grier, C. J., Trump, J. R., Shen, Y., et al. 2017, *ApJ*, 851, 21
 Guo, H., Sun, M., Liu, X., et al. 2019, *ApJL*, 883, L44
 Ho, L. C., Goldoni, P., Dong, X.-B., Greene, J. E., & Ponti, G. 2012, *ApJ*, 754, 11
 Hryniewicz, K., Czerny, B., Pych, W., et al. 2014, *A&A*, 562, A34
 Kaspi, S., Smith, P. S., Netzer, H., et al. 2000, *ApJ*, 533, 631
 Kokubo, M., Morokuma, T., Minezaki, T., et al. 2014, *ApJ*, 783, 46
 Korista, K., Kodituwakku, N., Corbin, M., & Freudling, W. 2004, in ASP Conf. Ser. 311, AGN Physics with the Sloan Digital Sky Survey, ed. G. T. Richards & P. B. Hall (San Francisco, CA: ASP), 415
 Korista, K. T., & Goad, M. R. 2000, *ApJ*, 536, 284
 Korista, K. T., & Goad, M. R. 2004, *ApJ*, 606, 749
 Korista, K. T., & Goad, M. R. 2019, *MNRAS*, 489, 5284
 LaMassa, S. M., Cales, S., Moran, E. C., et al. 2015, *ApJ*, 800, 144
 Landt, H., Ward, M. J., Kynoch, D., et al. 2019, *MNRAS*, 489, 1572
 Li, S.-L., & Cao, X. 2008, *MNRAS*, 387, L41
 Lyubarskii, Y. E. 1997, *MNRAS*, 292, 679
 MacLeod, C. L., Green, P. J., Anderson, S. F., et al. 2019, *ApJ*, 874, 8
 MacLeod, C. L., Ross, N. P., Lawrence, A., et al. 2016, *MNRAS*, 457, 389
 Mathews, W. G., & Ferland, G. J. 1987, *ApJ*, 323, 456
 Metzroth, K. G., Onken, C. A., & Peterson, B. M. 2006, *ApJ*, 647, 901
 Modzelewska, J., Czerny, B., Hryniewicz, K., et al. 2014, *A&A*, 570, A53
 Nenkova, M., Sirocky, M. M., Nikutta, R., Ivezić, Ž., & Elitzur, M. 2008, *ApJ*, 685, 160
 O'Brien, P. T., Goad, M. R., & Gondhalekar, P. M. 1995, *MNRAS*, 275, 1125
 Osterbrock, D. E. 1989, *Astrophysics of Gaseous Nebulae and Active Galactic Nuclei* (Sausalito, CA: University Science Books)
 Park, D., Woo, J.-H., Treu, T., et al. 2012, *ApJ*, 747, 30
 Pei, L., Fausnaugh, M. M., Barth, A. J., et al. 2017, *ApJ*, 837, 131
 Perez, E., Robinson, A., & de La Fuente, L. 1992, *MNRAS*, 256, 103
 Peterson, B. M. 2014, *SSRv*, 183, 253
 Peterson, B. M., Ferrarese, L., Gilbert, K. M., et al. 2004, *ApJ*, 613, 682
 Peterson, B. M., & Wandel, A. 1999, *ApJL*, 521, L95
 Popović, L. Č., Kovačević-Dojčinović, J., & Marčeta-Mandić, S. 2019, *MNRAS*, 484, 3180
 Rakić, N., La Mura, G., Ilić, D., et al. 2017, *A&A*, 603, A49

- Reichert, G. A., Rodriguez-Pascual, P. M., Alloin, D., et al. 1994, *ApJ*, 425, 582
- Richards, G. T., Lacy, M., Storrie-Lombardi, L. J., et al. 2006, *ApJS*, 166, 470
- Roig, B., Blanton, M. R., & Ross, N. P. 2014, *ApJ*, 781, 72
- Rumbaugh, N., Shen, Y., Morganson, E., et al. 2018, *ApJ*, 854, 160
- Runco, J. N., Cosens, M., Bennert, V. N., et al. 2016, *ApJ*, 821, 33
- Runnoe, J. C., Cales, S., Ruan, J. J., et al. 2016, *MNRAS*, 455, 1691
- Shen, Y. 2013, *BASI*, 41, 61
- Shen, Y., Brandt, W. N., Dawson, K. S., et al. 2015, *ApJS*, 216, 4
- Shen, Y., Greene, J. E., Strauss, M. A., Richards, G. T., & Schneider, D. P. 2008, *ApJ*, 680, 169
- Shen, Y., Horne, K., Grier, C. J., et al. 2016, *ApJ*, 818, 30
- Shen, Y., Richards, G. T., Strauss, M. A., et al. 2011, *ApJS*, 194, 45
- Sheng, Z., Wang, T., Jiang, N., et al. 2017, *ApJL*, 846, L7
- Sun, M., Trump, J. R., Shen, Y., et al. 2015, *ApJ*, 811, 42
- Trevese, D., Paris, D., Stirpe, G. M., Vagnetti, F., & Zitelli, V. 2007, *A&A*, 470, 491
- Vanden Berk, D. E., Richards, G. T., Bauer, A., et al. 2001, *AJ*, 122, 549
- Woo, J.-H. 2008, *AJ*, 135, 1849
- Yang, Q., Shen, Y., Chen, Y.-C., et al. 2019, arXiv:1904.10912
- Yang, Q., Wu, X.-B., Fan, X., et al. 2018, *ApJ*, 862, 109